

Continuous three-dimensional varifocal of vortex beams with twisted metasurfaces

Yiyi Li(黎仪艺), Wangzhe Zhou(周王哲), Shaoqi Li(李少奇), Xiaoyan Huang(黄晓艳), Fen Zhao(赵芬), Man Yuan(袁满), Jiagui Wu(吴加贵), Huan Chen(陈欢), Zhaojian Zhang(张兆健), and Junbo Yang (杨俊波)
Citation: Chin. Phys. B, 2026, 35 (**3**): 034208. DOI: 10.1088/1674-1056/adfc42
http://cpb.iphy.ac.cn; http://iopscience.iop.org/cpb

What follows is a list of articles you may be interested in

Fusion of fractional vortex pairs and their transition to integer vortex controlled by optical power

Chunzhi Sun(孙春志), Xiangwei Chen(陈向炜), Huizhong Xu, and Guo Liang(梁果)
Chin. Phys. B, 2025, 34 (**5**): 054202. DOI: 10.1088/1674-1056/adb8b9

Broadband polarization-independent terahertz multifunctional liquid crystal coding metasurface based on topological optimization

Yu Chen(陈羽), Wu-Hao Cao(曹吴昊), Jia-Qi Li(李嘉琦), Ming-Zhe Zhang(张明哲), Xin-Yi Du(杜欣怡), Ding-Shan Gao(郜定山), and Pei-Li Li(李培丽)
Chin. Phys. B, 2025, 34 (**4**): 044205. DOI: 10.1088/1674-1056/adad55

Diffraction deep neural network-based classification for vector vortex beams

Yixiang Peng(彭怡翔), Bing Chen(陈兵), Le Wang(王乐), and Shengmei Zhao(赵生妹)
Chin. Phys. B, 2024, 33 (**3**): 034205. DOI: 10.1088/1674-1056/ad0142

Ultraviolet metalens and metalens array of focused vortex beams

Jinping Zhang(张金平), Yan Wang(王焱), Huan Yuan(袁欢), Zehao Wang(王泽豪), Yang Deng(邓阳),Chengzhi Huang(黄承志), Jiagui Wu(吴加贵), and Junbo Yang(杨俊波)
Chin. Phys. B, 2023, 32 (**6**): 064206. DOI: 10.1088/1674-1056/ac9d87

Generation of elliptical airy vortex beams based on all-dielectric metasurface

Xiao-Ju Xue(薛晓菊), Bi-Jun Xu(徐弼军), Bai-Rui Wu(吴白瑞), Xiao-Gang Wang(汪小刚), Xin-Ning Yu(俞昕宁), Lu Lin(林露), and Hong-Qiang Li(李宏强)
Chin. Phys. B, 2023, 32 (**2**): 024215. DOI: 10.1088/1674-1056/ac7cd0

Continuous three-dimensional varifocal of vortex beams with twisted metasurfaces

Yiyi Li(黎仪艺)[1], Wangzhe Zhou(周王哲)[1], Shaoqi Li(李少奇)[1], Xiaoyan Huang(黄晓艳)[1], Fen Zhao(赵芬)[1,3], Man Yuan(袁满)[1], Jiagui Wu(吴加贵)[2], Huan Chen(陈欢)[1], Zhaojian Zhang(张兆健)[1], and Junbo Yang (杨俊波)[1,†]

[1] *College of Science, National University of Defense Technology (NUDT), Changsha* 410073, *China*
[2] *School of Physical Science and Technology Southwest University, Chongqing* 400715, *China*
[3] *School of Artificial Intelligence, Chongqing University of Technology, Chongqing* 401135, *China*

(Received 10 June 2025; revised manuscript received 22 July 2025; accepted manuscript online 18 August 2025)

Vortex beams with helical phase wavefronts and doughnut-shaped intensity profiles hold great promise for optical trapping, imaging, and quantum communication. However, dynamic control over their steering and focusing remains challenging with existing static generation methods. Here, we demonstrate a dynamic and compact moiré metasurfaces that enables full three-dimensional (3D) control over vortex beams. The paradigm incorporates a numerical unit cell model and an off-axis angular spectrum algorithm based on the generalized Snell's law of refraction in full space. The beam's transverse position and longitudinal focal length can be simultaneously controlled by integrating phase elements such as gratings, lenses, and spiral phase plates. This scheme offers a 12× large axial zoom range from 7.42 mm to 85.45 mm and a lateral steering capability of up to ±48 mm. The device exhibits an average side-mode suppression ratio of 27.3 and maintains a constant full width at half maximum over a 50° deflection range, preserving beam quality and directional stability during dynamic steering. This lightweight vortex beams solution may open new ways for dynamic beam shaping in super-resolution imaging, free-space communication, and biophotonics.

Keywords: vortex beams, light manipulation, tunable metasurfaces, moiré theory

PACS: 42.79.–e, 42.15.Eq, 42.50.Tx, 42.30.Ms

DOI: 10.1088/1674-1056/adfc42 **CSTR:** 32038.14.CPB.adfc42

1. Introduction

Structured light, with its freely tailorable amplitude, phase, and polarization distributions, offers unprecedented control over light matter interactions and the spatial shaping of optical fields.[1] Unlike conventional Gaussian beams, structured light modes, such as Bessel beams, Airy beams, and vector beams, exploit spatial degrees of freedom to enable novel functionalities in optical trapping, high-resolution imaging, and optical communication. Among these, vortex beams (VB) stand out due to their helical phase wavefronts, doughnut-shaped intensity profiles, and orbital angular momentum (OAM).[2] Since the theoretical introduction of optical OAM by Allen *et al*. in 1992,[3] vortex beams have unlocked new possibilities in quantum information science, high-capacity data transmission, and micro-manipulation. The intrinsically high-dimensional nature of OAM modes provides a rich Hilbert space for encoding information, establishing a foundation for next-generation photonic technologies. Continued advances in the generation, manipulation, and application of vortex light have since propelled a wide array of emerging applications across both classical and quantum domains.[4–7]

Traditionally, vortex beams have been generated and controlled using various methods, including spiral phase plates (SPPs),[8–10] computer-generated holography,[11,12] q-plates,[13,14] and spatial light modulators (SLMs).[15,16] These approaches typically rely on phase modulation through the propagation of light in continuous media, such as lenses or wave plates, to imprint the desired helical wavefront. However, such conventional techniques are inherently constrained by the physical size, material limitations, and structural complexity of bulk optical components.[17] As a result, they face challenges in scalability, efficiency, and dynamic tunability. In particular, vortex beams produced through these static methods often possess fixed topological charges and modal structures, such as Laguerre–Gaussian or Bessel beam profiles,[18,19] making them ill-suited for applications requiring adaptability to dynamic environments.

In recent years, metasurfaces, planar, and two-dimensional (2D) structures, composed of periodic arrays of subwavelength-scale meta-atoms, have emerged as a powerful platform for the precise and efficient manipulation of light.[20] These ultrathin optical elements have revolutionized the generation and control of structured light, offering unprecedented flexibility that extends far beyond the capabilities of traditional bulk optics. Owing to their compact form factor, low weight, cost-effectiveness, and ease of integration, metasur-

†Corresponding author. E-mail: yangjunbo@nudt.edu.cn

© 2026 Chinese Physical Society and IOP Publishing Ltd. All rights, including for text and data mining, AI training, and similar technologies, are reserved.

faces have enabled a new class of miniaturized optical systems and found widespread application in imaging,[21,22] optical camouflage,[23,24] holographic displays,[25,26] and quantum information processing.[27,28] In particular, metasurfaces have shown extraordinary potential in the generation and control of structured light. Metasurfaces have been used to generate vortex beams with arbitrary integer and fractional topological charges,[29] create Bessel beam arrays through Huygens metasurfaces by combining Dammann grating and axicon functionalities,[30] and realize three-dimensional (3D) multi-target holographic encryption via OAM multiplexed holography.[31] Furthermore, the multi-degree-of-freedom design inherent to metasurfaces facilitates multidimensional coupling of OAM with polarization and wavelength,[32] opening new avenues for high-capacity optical communication and quantum encoding. These advances break limitations that exist in conventional optics so far and cannot be replaced by conventional optics or other wavefront modulation tools.

As the field of metasurfaces continues to evolve, there is a growing demand for multifunctional and dynamically reconfigurable devices to meet the requirements of next generation photonic applications.[33] However, once fabricated, conventional metasurfaces exhibit fixed structural geometries and optical responses, limiting their dynamic adaptability. To address this challenge, a variety of tunable platforms have been explored, including phase change materials,[25,34] graphene,[35] liquid crystals,[36,37] and micro electromechanical systems (MEMS).[38] These technologies have enabled important breakthroughs in applications such as optical communication, optical trapping, microscopy, and LiDAR. Nevertheless, their integration often involves trade-offs in complexity, cost, scalability, or response speed, posing barriers to widespread deployment. Given the unique properties of vortex beams, including their helical phase wavefronts and annular intensity profiles coupled with their intrinsic orbital angular momentum, there is increasing interest in leveraging them for disruptive applications in quantum communication, superresolution imaging, and optical manipulation. These demands underscore an urgent need for compact systems capable of efficiently generating vortex beams while enabling dynamic beam steering and focal tuning in a unified and reconfigurable platform.

The integration of moiré-effect-based optical devices offers a novel and versatile approach for achieving continuous 3D control of vortex beams. First proposed by Bernet *et al*. in 2008,[39] moiré structures are composed of two or more cascaded diffractive optical elements, where the output wavefront can be dynamically reshaped through relative rotational alignment. By carefully designing the surface phase profiles of each layer, moiré optical elements can continuously tune the behavior of conventional components such as zoomable Fresnel lenses,[40] axicons, and spiral phase plates with adjustable topological charges.[41] Metasurfaces, with their ultrathin form factor, high design freedom, and fabrication compatibility, present a compelling alternative to traditional diffractive optical elements. When configured in a moiré architecture, metasurfaces have demonstrated remarkable application potential in areas such as constant-magnification fluorescence microscopy,[42] full-spectrum computational imaging,[43] augmented reality (AR) systems,[44] and optical edge detection.[45] Of particular interest is their capability to modulate structured light fields. For instance, moiré metasurfaces have enabled the dynamic tuning of vortex beam topological charges,[46] lateral steering of Airy beams,[47] and control over the order and nondiffracting length of Bessel beams.[48] Moreover, by leveraging rotational control, vortex beams with distinct topological charges can be spatially separated into different channels, enabling multi-channel signal routing.[49] When combined with polarization multiplexing, such platforms can simultaneously tune the vortex beam's topological charge across a range from -3 to $+3$ while also adjusting its vector polarization state.[50] Notably, the moiré effect offers an inherently broadband and scalable approach, with demonstrated applicability across the visible,[51] microwave,[52] and terahertz[53] regimes, and even extends to the manipulation of acoustic waves.[54] These capabilities position moiré metasurfaces platforms as a powerful solution for dynamic wavefront engineering in both photonic and phononic systems.

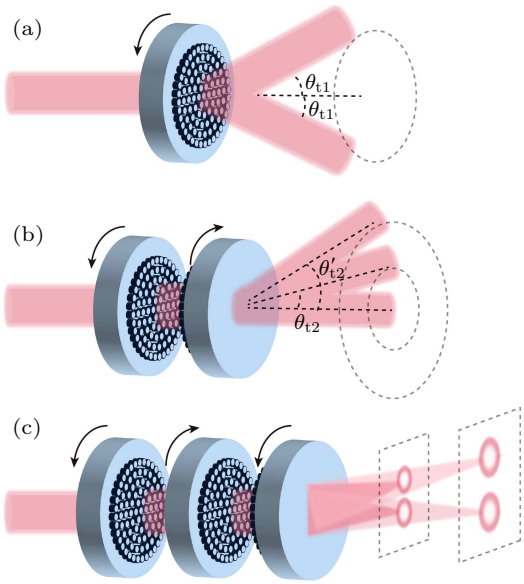


Fig. 1. The schematics of the twisted metasurfaces. (a) A single-layer twisted metasurface enables one-dimensional beam steering with a fixed elevation angle, denoted as θ_{t1}. (b) A double-layer twisted metasurfaces supports continuous 2D lateral beam deflection. (c) The three-layer twisted metasurfaces, which integrates a moiré zoom lens with a double-layer twisted system shown in panel (b), enables full 3D steering of vortex beams.

Here, we propose a twisted metasurfaces-based strategy that integrates gratings, dynamic focusing, and spiral phase

modulation to enable flexible control of vortex beams at arbitrary positions in 3D space. This approach combines the principles of generalized Snell's law throughout the full space with plane wave angular spectrum theory to achieve comprehensive beam shaping. As a proof of concept, we demonstrate three moiré metasurfaces devices capable of structured beam manipulation in one, two, and three dimensions. A single-layer twisted metasurface is employed to achieve one-dimensional beam steering, while a double-layer twisted metasurfaces enables unrestricted 2D lateral deflection, maintaining high optical throughput throughout the tuning range. The three-layer twisted metasurfaces, which integrates a moiré zoom lens with a double-layer twisted system, achieves simultaneous zooming and steering of vortex beams in three-dimensional space. Schematics of these three metasurfaces configurations are illustrated in Fig. 1. This multifunctional platform is expected to advance applications in optical communication, optical trapping, and super-resolution imaging.

2. Designs and principles

When an incident beam sequentially passes through each layer of the twisted metasurfaces, its propagation direction and the focal position can be continuously modulated via rotational tuning. The interaction of light with a single-layer metasurface is governed by the generalized Snell's law, which describes the anomalous refraction induced by spatially varying phase gradients. By decomposing the wavevector components in the 3D space, different forms of 2D [20] or 3D[55,56] expressions can be obtained. For simplicity and generality, we adopt the 3D formulation illustrated in Fig. 2(a). When the incident and refracted rays do not lie in the same plane, the corresponding wavevectors can be expressed as $\boldsymbol{k}_{\mathrm{i}} = k_0 n_{\mathrm{i}} [\sin(\theta_{\mathrm{i}})\cos(\phi_{\mathrm{i}}), \sin(\theta_{\mathrm{i}})\sin(\phi_{\mathrm{i}}), \cos(\theta_{\mathrm{i}})]$ and $\boldsymbol{k}_{\mathrm{t}} = k_0 n_{\mathrm{t}} [\sin(\theta_{\mathrm{t}})\cos(\phi_{\mathrm{t}}), \sin(\theta_{\mathrm{t}})\sin(\phi_{\mathrm{t}}), \cos(\theta_{\mathrm{t}})]$, where $k_0 = 2\pi/\lambda_0$ is the vacuum wave number, λ_0 is the free-space wavelength, and n_{i} and n_{t} are the refractive indices of the isotropic, homogeneous media on the incident and transmission sides of the metasurface, respectively. The angular orientation of the wavevector $\boldsymbol{k}$ is defined by the elevation angle θ, which describes the angle between $\boldsymbol{k}$ and the optical axis (z axis), and the azimuthal angle ϕ, which is the angle between the projection of $\boldsymbol{k}$ onto the xy-plane and the x axis. These angles satisfy the normalization condition $[\sin(\theta)\cos(\phi)]^2 + [\sin(\theta)\sin(\phi)]^2 + \cos^2(\theta) \equiv 1$. Assuming that the local phase distribution of the metasurface is denoted by Φ, the generalized law of refraction in full 3D space can be written as

$$n_{\mathrm{t}}\sin(\theta_{\mathrm{t}})\cos(\phi_{\mathrm{t}}) = n_{\mathrm{i}}\sin(\theta_{\mathrm{i}})\cos(\phi_{\mathrm{i}}) + \frac{\lambda_0}{2\pi}\frac{\partial\Phi}{\partial x}, \tag{1}$$

$$n_{\mathrm{t}}\sin(\theta_{\mathrm{t}})\sin(\phi_{\mathrm{t}}) = n_{\mathrm{i}}\sin(\theta_{\mathrm{i}})\sin(\phi_{\mathrm{i}}) + \frac{\lambda_0}{2\pi}\frac{\partial\Phi}{\partial y}. \tag{2}$$

For cascaded metasurfaces design in this work, we assume that $n_{\mathrm{i}} = n_{\mathrm{t}} = 1$, and $\theta_{\mathrm{i}} = 0$, the generalized Snell's law of refraction simplifies to

$$\frac{2\pi}{\lambda_0}\sin(\theta_{\mathrm{t}})\cos(\phi_{\mathrm{t}}) = \frac{\partial\Phi}{\partial x}, \tag{3}$$

$$\frac{2\pi}{\lambda_0}\sin(\theta_{\mathrm{t}})\sin(\phi_{\mathrm{t}}) = \frac{\partial\Phi}{\partial y}. \tag{4}$$

In order to control the deflection of the light beam, we designed a twisted metasurface as a demonstration and set its phase distribution to $\Phi_1(\varphi, r)$:

$$\Phi_1(\varphi, r) = Ck_0 r\sin(\varphi) = Ck_0 y, \tag{5}$$

where C is a constant with a value range of $(-1, 1)$. (φ, r) is the polar angle and radius of the unit structure on the metasurface with the center of the metasurface as the origin. The metasurface is rotated clockwise by θ_1, and the phase distribution after rotation corresponds to formulas (3) and (4), and the deflection angle of the outgoing light beam is obtained

$$\phi_{\mathrm{t1}} = \frac{\pi}{2} + \theta_1, \tag{6}$$

$$\theta_{\mathrm{t1}} = \arcsin(C). \tag{7}$$

This shows that the elevation angle θ_{t1} of the light beam emitted from the metasurface model is always a fixed value, namely $\arcsin(C)$, and the azimuth angle ϕ_{t1} rotates with the rotation of the metasurface θ_1, and the deflection trajectory on the emission plane is a circle.

To achieve arbitrary two-dimensional beam steering on the output plane, we design a twisted double-layer metasurfaces structure that leverages the moiré effect. Let the phase profiles of the two metasurfaces be designed as Φ_2 and Φ_3, respectively. When the spacing between the two layers is sufficiently small, diffraction effects in the intermediate gap can be neglected.

$$\begin{aligned}\Phi_2(\varphi, r) &= Ck_0 r\sin(\varphi) = Ck_0 y,\\ \Phi_3(\varphi, r) &= -Ck_0 r\sin(\varphi) = -Ck_0 y.\end{aligned} \tag{8}$$

The first metasurface rotates clockwise by θ_2, and the second metasurface rotates clockwise by θ_3. Comparing with Snell's law in the whole space, the relationship between the rotation angles θ_2, θ_3 and the deflection directions of the outgoing beams θ_{t2}, ϕ_{t2} can be obtained, which can be expressed as follows:

$$\begin{aligned}&\frac{2\pi}{\lambda_0}\sin(\theta_{\mathrm{t2}})\cos(\phi_{\mathrm{t2}})\\ &= \frac{\partial\Phi_{\mathrm{com}}}{\partial x} = 2Ck_0\sin\left(\frac{\theta_3-\theta_2}{2}\right)\cos\left(\frac{\theta_3+\theta_2}{2}\right),\\ &\frac{2\pi}{\lambda_0}\sin(\theta_{\mathrm{t2}})\sin(\phi_{\mathrm{t2}})\\ &= \frac{\partial\Phi_{\mathrm{com}}}{\partial y} = 2Ck_0\sin\left(\frac{\theta_3-\theta_2}{2}\right)\sin\left(\frac{\theta_3+\theta_2}{2}\right).\end{aligned} \tag{9}$$

The numerical solution can be directly obtained from the above equation, and one possible solution can be expressed as (as shown in Fig. 2(b)):

$$\theta_{t2} = \arcsin\left[2C\sin\left(\frac{\theta_3-\theta_2}{2}\right)\right],$$
$$\phi_{t2} = \frac{\theta_3+\theta_2}{2}. \tag{10}$$

Here, when the value range of θ_2 and θ_3 is $(-180°, 180°)$, the corresponding scanning range of the outgoing beam on the 2D plane is

$$\begin{cases} \theta_{t2} \in [-\theta_{max}, \theta_{max}], \\ \phi_{t2} \in [-180°, 180°], \end{cases}$$

where the maximum elevation angle of the outgoing beam is $\theta_{max} = \arcsin(2C)$.

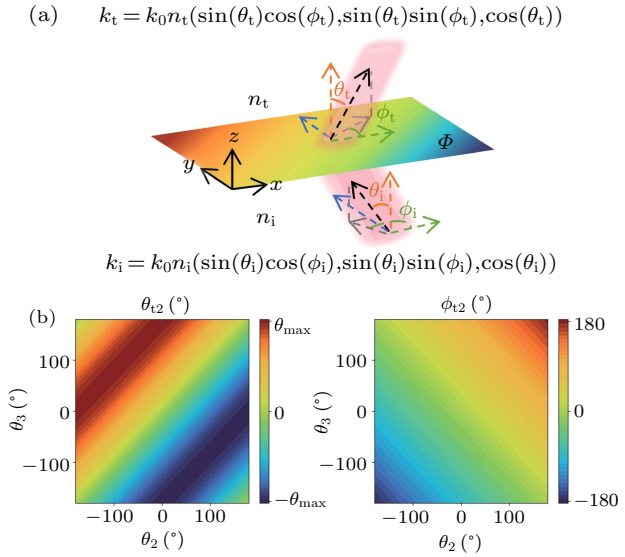


Fig. 2. (a) Generalized Snell's law of refraction in 3D space. A metasurface with a phase profile Φ modifies the trajectory of an incident wave at the interface between isotropic homogeneous media with refractive indices n_i and n_t. The rainbow-colored gradient denotes the spatial phase distribution. The incident and refracted wave vectors are k_i and k_t, respectively. (b) Functional relationship between the rotation angles θ_2 and θ_3 of the twisted double-layer metasurface and the resulting polar angle θ_{t2} and azimuthal angle ϕ_{t2} of the output beam.

In order to design a 3D zoom metadevice, we cascaded three metasurfaces, and the phase distributions of the three cascaded metasurfaces are $\Phi_4(\varphi,r)$, $\Phi_5(\varphi,r)$, and $\Phi_6(\varphi,r)$, respectively. The principle of phase superposition is used to combine the functions of on-axis zoom and deflection control with the spiral phase plate.

In order to control the zoom of the beam in the optical axis direction (z-axis), we designed the following phase profile

$$\Phi_a(\varphi,r) = \frac{r^2}{\lambda f_0}\varphi,$$
$$\Phi_b(\varphi,r) = -\frac{r^2}{\lambda f_0}\varphi. \tag{11}$$

Here, f_0 is the reference focal length. When the two metasurfaces rotate relative to each other by θ, combined with the phase of the lens $T_{lens} = \exp\left(-i\frac{\pi r^2}{\lambda}f\right)$, the adjustable focal length is obtained

$$f = \frac{\pi f_0}{\theta}. \tag{12}$$

Although both quadratic and hyperbolic phase profiles can achieve focusing, in our case, the quadratic phase yields a near-linear and analytically tractable relationship between the relative rotation angle and the effective focal length (as expressed in Eq. (12)). Moreover, when used as the phase distribution for moiré metasurface layers, the quadratic phase introduces smaller deviations compared to the hyperbolic phase,[57] making it more suitable for our design under the given conditions.

In order to make the vortex light realize the beam deflection function while zooming, we superimpose the phases of $\Phi_2(\varphi,r)$, $\Phi_3(\varphi,r)$ with $\Phi_a(\varphi,r)$, and $\Phi_b(\varphi,r)$. The phase distribution of the three cascaded metasurfaces that realizes the three-dimensional zoom of the vortex light can be expressed as

$$\begin{aligned} \Phi_4(\varphi,r) &= \Phi_2(\varphi,r) = Ck_0 r\sin(\varphi), \\ \Phi_5(\varphi,r) &= \Phi_3(\varphi,r) + \Phi_b(\varphi,r) \\ &= -Ck_0 r\sin(\varphi) - \frac{r^2}{\lambda f_0}\varphi, \\ \Phi_6(\varphi,r) &= \Phi_a(\varphi,r) + l\varphi = \frac{r^2}{\lambda f_0}\varphi + l\varphi. \end{aligned} \tag{13}$$

The cascaded structure of the three metasurfaces functions equivalently to an off-axis vortex metalens with tunable focal length and steering capability. Specifically, when the third metasurface (MS3) is rotated relative to the second metasurface (MS2), the system exhibits a zooming effect. Conversely, rotating the first metasurface (MS1) relative to MS2 enables beam steering through angular deflection. When all three metasurfaces are rotated at different angles, the composite system achieves simultaneous focal length tuning and off-axis beam control. In this work, the metasurfaces act as phase-only periodic elements. We design the system's overall phase response by engineering the phase transfer functions of individual layers. Figure 3 illustrates the phase distributions of the individual metasurfaces and their combined response under various relative rotation states. In the first configuration, where MS1 and MS2 remain fixed while MS3 is rotated clockwise by 10°, the system forms an on-axis metalens with a focal length of $18f_0$. Increasing the rotation of MS3 to 30° reduces the focal length to $6f_0$, maintaining on-axis focusing. In a third scenario, MS3 remains fixed while MS1 is rotated clockwise by 30° and MS2 is rotated counterclockwise by 30°, resulting in off-axis focusing. Since MS3 retains a 30° clockwise rotation relative to MS2, the focal length remains constant at $6f_0$. However, the additional 60° relative rotation between MS1 and MS2 introduces angular steering, yielding

a deflection in elevation angle of $\arcsin[2C\sin(30^\circ)$ while the azimuthal angle remains 0°. In the fourth scenario, the relative rotation between MS3 and MS2 is maintained at 30°, ensuring the same focal length as in the third case. Meanwhile, the relative rotation angle between MS1 and MS2 is increased to 120°, further enhancing the deflection angle of the output beam.

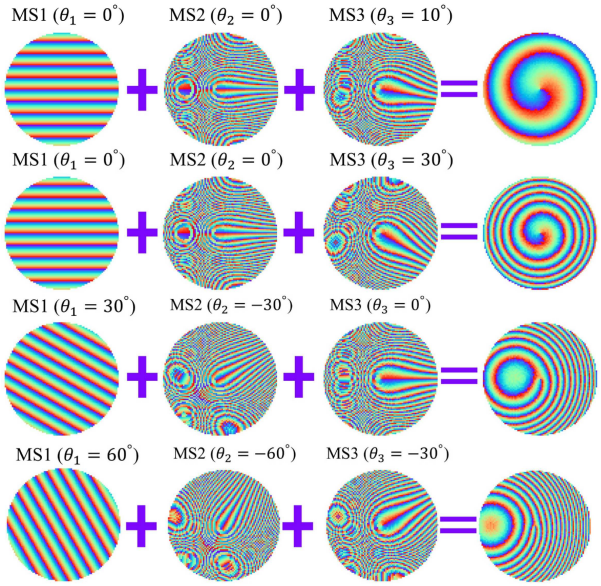


Fig. 3. Phase distribution of three-layer twisted metasurfaces with vortex light 3D zoom and its cascade phase distribution.

3. Results and discussion

As described in Eq. (13), the constants C and f_0 are pivotal in enabling beam deflection and zooming via the twisted metasurfaces system. Specifically, C governs the maximum deflection angle of the output beam, while f_0 defines the focusing position of the light beam. In our case, the incident wavelength is set to 633 nm, and the diameter of metasurface is 1 mm. Each metasurface is composed of cylindrical nanopillars with varying diameters to achieve a full 2π phase coverage, independent of polarization. The unit cell consists of Si_3N_4 nanopillars with a height of 900 nm (H) and a period of 250 nm (P), fabricated on an SiO_2 substrate. The pillar diameters D range from 100 nm to 240 nm. As a proof-of-concept demonstration, achieving full 2π phase modulation and high optical transmittance is essential to approximate the ideal phase profile and ensure high-fidelity wavefront control. Currently, silicon nitride and titanium dioxide,[58,59] as CMOS-compatible, high-band-gap dielectrics, offer excellent transparency over the visible to near-infrared range ($\sim$ 400 nm–900 nm), making them attractive platforms for low-loss, high-efficiency metasurfaces. Prior studies have demonstrated that Si_3N_4 nanopillars with comparable aspect ratios can be reliably fabricated using advanced nanofabrication techniques such as electron-beam lithography[60] and inductively coupled plasma (ICP) fluorine etching.[61] Therefore, we believe that the functionalities demonstrated in this work can be feasibly realized using current nanofabrication processes. Lumerical FDTD Solutions is used to characterize the optical response of the nanopillar unit cells. By changing the diameter D of the cylinder, the phase of the transmitted light can be modulated from $-\pi$ to π, while the average transmittance is 97%, keeping the transmission amplitude close to 1. The simulated phase and amplitude responses of the unit cell are shown in Fig. 4. To ensure that the beam remains confined within the optical path between the cascaded metasurfaces, we choose $C = 0.3$ and $f_0 = 2.5$. To ensure effective moiré pattern formation, the spacing between metasurfaces is maintained below the Talbot distance;[39] in this work, it is set to 200 nm, allowing the diffracted wavefronts to spatially overlap and interact as intended. This requirement is experimentally feasible. Moreover, this value can be further scaled by increasing the metasurface period or by reducing the operating wavelength, depending on the specific design objectives. Prior studies have demonstrated spacing control using deposited SiO_2 layers,[57] phase retrieval methods based on the Huygens–Fresnel principle,[62] ray-tracing back-design approaches,[56] and complex optical alignment strategies for multi-plane imaging.[63,64]

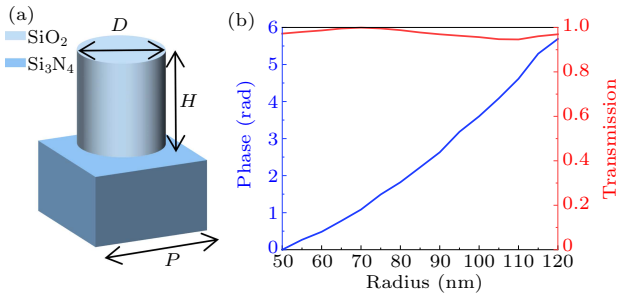


Fig. 4. Details about the numerical simulation of the metasurface unit cell.

3.1. Beam steering control

The beam deflection performance of the twisted metasurfaces is evaluated through numerical simulations performed in Lumerical FDTD Solutions. The computational grid is automatically generated by the simulation software, and perfectly matched layer (PML) boundary conditions are applied on all sides to eliminate spurious reflections and ensure the energy conservation. To evaluate angular steering, we rotate a single-layer twisted metasurface from 0° to 360° in 30° increments. At each step, we compute the far-field electric field intensity distribution. The regions with the intensity below 10% of the peak value are excluded, and the integrated intensity is plotted, as shown in Fig. 5(a).

The relationship between the rotation angle of the single-layer twisted metasurface and the output beam direction based

on simulation results is summarized in Table 1. θ_1 refers to the rotation angle of a single-layer metasurface. θ_{t1} and ϕ_{t1} denote the elevation angle and the azimuth angle of the output beam, respectively. According to Eq. (7), the elevation angle θ_{t1} of the outgoing beam remains constant at $\arcsin(C)$. In our design, we set $C = 0.3$, giving $\theta_{t1} \approx 17.46°$. As the metasurface rotates, the azimuthal angle of the outgoing beam varies in accordance with Eq. (6), enabling continuous one-dimensional (1D) beam steering. The average optical transmittance of the single-layer metasurface is 93.85%.

To further validate the 2D beam steering capability, we employ a double-layer twisted metasurfaces. As illustrated in Fig. 5(b), the far-field intensity distributions at a projection distance of 1 m are presented for 35 representative cases. The relationship between the rotation angles of the two-layer metasurfaces and the deflection angles of the output beam is summarized in Table 2.

Table 1. Simulated output beam parameters corresponding to different rotation angles of the single-layer twisted metasurface.

No.	θ_1 (°)	(θ_{t1}, ϕ_{t1}) (°, °)	No.	θ_1 (°)	(θ_{t1}, ϕ_{t1}) (°, °)	No.	θ_1 (°)	(θ_{t1}, ϕ_{t1}) (°, °)
1	0	(17.25, 89.03)	5	–120	(17.46, –30.38)	9	120	(17.46, –149.62)
2	–30	(17.46, 59.62)	6	–150	(17.46, –59.62)	10	90	(17.46, 179.03)
3	–60	(17.46, 30.38)	7	–180	(17.46, –89.03)	11	60	(17.46, 150.38)
4	–90	(17.46, 0.97)	8	150	(17.46, –120.38)	12	30	(17.46, 120.38)

Table 2. Simulated output beam parameters corresponding to different rotation angles of the double-layer twisted metasurface.

No.	(θ_1, θ_2) (°, °)	(θ_{t1}, ϕ_{t1}) (°, °)	No.	(θ_1, θ_2) (°, °)	(θ_{t1}, ϕ_{t1}) (°, °)
	(0, 0)	(0.41, 135.0)	18	(–115, –65)	(14.85, –91.12)
1	(–10, 10)	(6.06, –2.73)	19	(45, 135)	(24.65, 90.69)
2	(–25, 25)	(14.85, 1.12)	20	(–15, –105)	(25.2, 120.5)
3	(–45, 45)	(25.29, –0.67)	21	(15, –75)	(25.2, 149.5)
4	(–60, 60)	(31.18, 0.56)	22	(75, –15)	(25.2, –149.5)
5	(–90, 90)	(36.73, –0.48)	23	(105, 15)	(25.2, –120.5)
6	(10, –10)	(6.06, –177.27)	24	(–135, –45)	(24.65, –89.31)
7	(25, –25)	(14.85, 178.88)	25	(–105, –15)	(25.2, –59.5)
8	(45, –45)	(25.29, –179.33)	26	(–75, 15)	(25.2, –30.5)
9	(60, –60)	(31.17, 179.44)	27	(–15, 75)	(25.2, 30.5)
10	(90, –90)	(36.73, –179.52)	28	(15, 105)	(25.2, 59.5)
11	(–80, –100)	(6.06, 87.27)	29	(–105, 15)	(31.25, –45.0)
12	(100, 80)	(6.06, –92.73)	30	(–180, 0)	(36.73, –90.48)
13	(–35, –55)	(6.12, 135.0)	31	(105, –15)	(31.25, –135.0)
14	(55, 35)	(6.12, –135.0)	32	(15, –105)	(31.25, 135.0)
15	(–55, –35)	(6.12, –45.0)	33	(0, 180)	(36.73, 90.48)
16	(35, 55)	(6.12, 45.0)	34	(–15, 105)	(31.25, 45.0)
17	(65, 115)	(14.85, 88.88)			

Here, θ_1 and θ_2 represent the rotation angles of the first and second metasurface layers, respectively, while θ_{t1} and ϕ_{t1} denote the elevation and azimuth angles of the output beam. The elevation angles span from 0° to 36°, and the azimuth angles range from $-180°$ to 180°, demonstrating the metasurfaces' ability to direct beams across a wide angular range. The beam can be steered to arbitrary positions within the two-dimensional output plane, and the theoretical maximum elevation angle of $\theta_{max} = \arcsin(2C) = 36.87°$ is achieved. The double-layer twisted metasurface exhibits an average transmittance of 87%. Compared to a single-layer design, the stacking of multiple metasurfaces generally leads to reduced efficiency due to increased scattering and interface losses. Figure 5(c) plots the normalized output intensity as a function of deflection angle for 11 selected cases (No. 0 to 10 in Fig. 5(b)). The results indicate that the beam maintains strong directivity, with the output power gradually decreasing as the deflection angle increases. To quantify beam quality, we calculate the side-mode suppression ratio (SMSR) and the full width at half maximum (FWHM). The FWHM is defined as the angular width at half the peak power of the main lobe. Within the deflection range of $-25°$ to 25°, the FWHM remains constant at 3.62°, indicating minimal beam divergence. When the deflection angle increases beyond 31°, the FWHM slightly broadens to 5.42°, suggesting a moderate degradation in beam confinement. The SMSR is further used to evaluate sidelobe suppres-

sion, defined as

$$\mathrm{SMSR} = 10\log_{10}\left(\frac{I_{\text{main lobe}}}{I_{\text{side lobe}}}\right). \tag{14}$$

The average side-mode suppression ratio (SMSR) of the beam steering device reaches 27.3, indicating minimal sidelobe energy and strong main lobe confinement. This level of performance is suited for high-precision optical systems and long-range beam delivery applications. Within the deflection range of $-15°$ to $15°$, the SMSR exceeds 30, further confirming the system's excellent directivity. By tuning design parameters and optimizing structural configurations, the cascaded metasurfaces can achieve even broader deflection ranges and enhanced beam quality, establishes a promising platform for the realization of three-dimensional zoom optics.

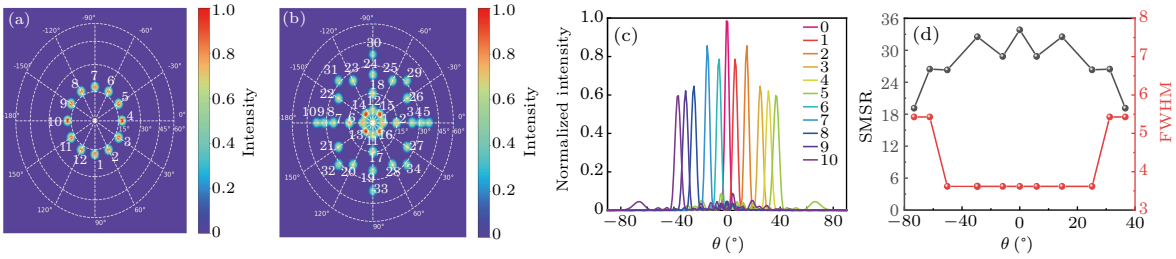


Fig. 5. Beam steering performance of twisted metasurfaces. (a) Simulated one-dimensional beam deflection controlled by a single-layer twisted metasurface. (b) The 2D beam steering realized using a cascaded double-layer twisted metasurfaces. The central reference point is labeled as 0. (c) Far-field power distribution as a function of elevation angle for selected cases (0–10) shown in panel (b). (d) Corresponding side-mode suppression ratio (SMSR) and full width at half maximum (FWHM) for cases 0–10, illustrating beam quality under varying deflection conditions.

3.2. On-axis zoom and off-axis focusing of vortex beams

To demonstrate the capability of the proposed cascaded metasurfaces architecture in manipulating vortex beams in 3D space, we design three cascaded metasurfaces based on Eq. (12), with $l = 1$. The light field intensity of the output beam is calculated using a plane-wave angular spectrum diffraction method. In this off-axis control scenario, the output aperture significantly exceeds the size of the input plane, rendering the conventional angular spectrum method unsuitable. As this method relies on a pair of Fourier transforms, it requires the input and output planes to be of equal dimensions. Simply enlarging the input window to match the output field would dramatically increase computational load and memory demand. To address this, we employ an improved off-axis angular spectrum algorithm,[65] optimized for propagating large-scale wavefronts that cannot be fully stored in memory simultaneously. The propagation of the optical wave in the off-axis configuration is illustrated in Fig. 6, where $u_0(x_0, y_0, 0)$ defines the field distribution at the input plane $(x_0, y_0, 0)$, and $u(x, y, z_0)$ denotes the field distribution at the observation plane (x, y, z_0) under monochromatic illumination of wavelength λ. This method accommodates both short- and long-distance propagation, and suppresses aliasing artifacts by bandwidth-limiting the transfer function and filtering high-frequency components that do not contribute to the desired optical field evolution.

To evaluate the zooming capability of the cascaded metasurfaces system, we fix the first and second metasurface and vary the rotation angle of the third metasurface from 0° to 60°, selecting five representative angles: 5°, 10°, 20°, 30°, and 60°, for demonstration. According to Eq. (13), the theoretical focal length is inversely proportional to the relative rotation angle, yielding focal lengths of $36f_0$ $18f_0$, $9f_0$, $6f_0$, and $3f_0$, respectively.

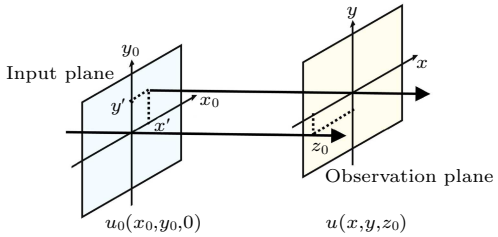


Fig. 6. Improved off-axis angular spectrum algorithm capable of computing optical fields on arbitrary planes in 3D space.

Figure 7 presents the normalized light field intensity distributions on the XOZ plane. White dashed lines indicate the focal planes. As the rotation angle increases, the focal length decreases accordingly, and the simulated focal positions closely match the theoretical values. Specifically, the focal lengths achieved for the selected rotation angles are 85.45 mm, 43.64 mm, 22.27 mm, 14.85 mm, and 7.42 mm, corresponding to a 12× continuous zoom ratio. At larger rotation angles, the device exhibits shorter focal lengths, stronger focusing, higher energy concentration, and reduced depth of field. In contrast, smaller rotation angles produce longer focal lengths, broader focal spots, more dispersed energy, and increased depth of field. This behavior arises from the increase in numerical aperture associated with larger rotation angles, which enhances the focusing capability of the vortex beam while keeping the input aperture constant. The central column of Fig. 7 shows the transverse light field distributions on the XOY plane at each focal plane. As expected for a vortex beam with topological charge $l = 1$, the intensity profiles exhibit characteristic donut-shaped patterns with a central dark core, an optical singularity. As the rotation angle increases, the dark core contracts and the

radius of the surrounding intensity ring decreases. The rightmost column of Fig. 7 shows the corresponding phase distributions, revealing a helical phase profile with a single 2π cycle, confirming the generation of a first-order vortex beam. For the triple-layer configuration, the average transmittance decreases to around 73%. This gradual reduction in transmittance with increasing number of layers is primarily attributed to additional scattering, interface reflections, and cumulative fabrication imperfections.

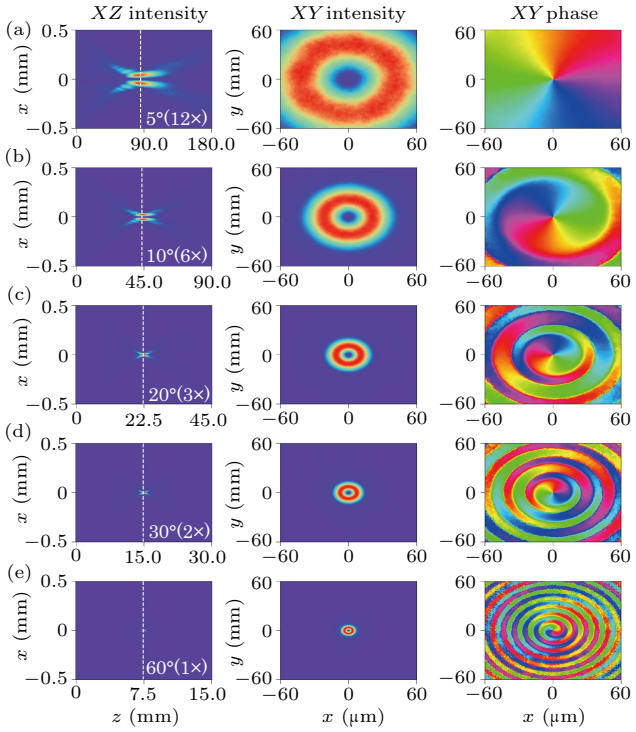


Fig. 7. Zoom control along the vortex beam axis. Intensity and phase distributions of the output field for relative rotation angles of MS3 with respect to MS2 of (a) 5°, (b) 10°, (c) 20°, (d) 30°, and (e) 60°. For each case, the left subpanel shows the light intensity distribution on the *xz* plane, the center subpanel presents the transverse intensity distribution on the *xy* plane at the focal plane (the dashed line in the *xz* plane), and the right subpanel displays the corresponding phase distribution on the same focal plane.

To demonstrate the device's capability for three-dimensional tunable vortex beam focusing, we first verify its longitudinal (z-axis) focal length adjustment. Simultaneously, we assess transverse plane focusing control by independently manipulating the relative rotations between metasurfaces. Specifically, the relative rotation between MS2 and MS3 modulates the focal length of the cascaded device, while the rotation between MS1 and MS2 controls the deflection angle of the output beam. Taking the long-focus (12×) and short-focus (1×) states, achieved by rotating MS3 by 5° and 60° relative to MS2, respectively, as examples, we select nine target positions on each focal plane (labeled 0 to 8 for 12×, and 9 to 17 for 1×) to evaluate device performance (as shown in Figs. 8(a) and 8(b)). Insets display the vortex beam intensity profiles at these positions. By independently rotating each metasurface, the vortex beam is precisely steered to corresponding locations in 3D space, in excellent agreement with theoretical predictions from Eqs. (9) and (12). The device achieves a maximum dynamic control range of ±48 mm in the transverse plane and from 7.42 mm to 85.45 mm along the longitudinal axis. For both long- and short-focus states, vortex beams maintain symmetry at small deflection angles (highlighted by the purple circles in Figs. 8(a) and 8(b). As shown in Fig. 3, larger output deflection angles require steeper phase gradients at the edges of the cascaded phase profile. This increases the risk of undersampling, which can lead to aberrations,[66] and also highlights the inherent limitations of the global phase tuning mechanism.[67] As a result, asymmetric features appear in the vortex beam during the deflection process at larger angles, as illustrated in Fig. 8, causing asymmetry in the vortex beam profile that rotates with the metasurface orientation. Such aberrations can be mitigated by further optimization of the phase distribution parameters,[67] as well as by employing different phase engineering approaches[68] to improve edge sampling and compensate for the limitations of global phase tuning. Leveraging the moiré effect, the device attains large magnification and zoom capabilities, enabling even small-angle deflected vortex beams to access a broad spatial control range in three dimensions.

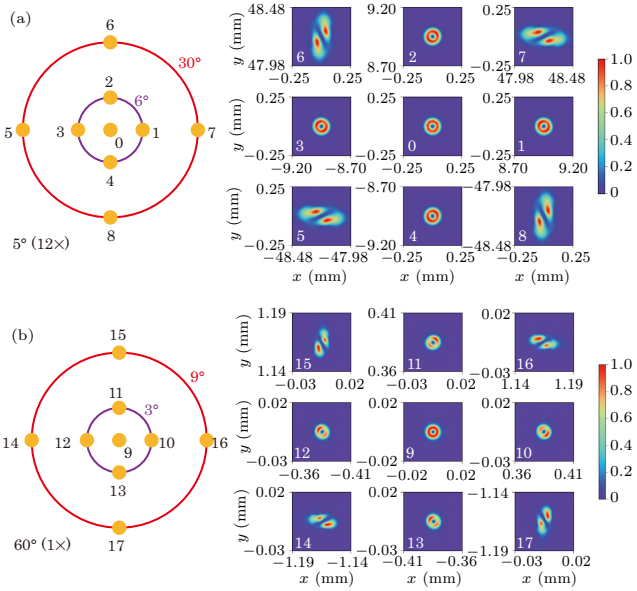


Fig. 8. Off-axis control of vortex light. Vortex beam intensity distributions on the transverse plane corresponding to MS3 rotation angles of (a) 5° and (b) 60° relative to MS2.

4. Conclusion

In summary, our work demonstrates the feasibility and potential of cascade metasurfaces based on the principle of moiré effect in the manipulation of vortex light. Using the phase distribution of gratings, lenses and spiral phase plates, we designed three cascade twisted metasurfaces, which are used to realize the functions of beam deflection, focusing and simultaneous deflection and focusing control of vortex light. We verified that the cascade device for beam deflection can

achieve a wide range of elevation deflection from 0° to 36° and azimuth angle control from −180° to 180°. And its control range can be further expanded with the setting of relevant parameters. In addition, the focal length control range of the cascade device used to control the zoom and deflection control of vortex light can achieve 12 times zoom (7.42 mm to 85.45 mm), and it has the ability to simultaneously control the movement of vortex light of arbitrary cross-section, and its maximum lateral dynamic control range is from −48 mm to 48 mm. While spatial light modulators (SLMs) can generate arbitrary programmable phase profiles and are often used to produce vortex beams, they are bulky and expensive, which limits their integration and flexibility in compact optical systems. Their operation depends on the reorientation of liquid crystal molecules under an electric field to modulate the incident light's phase via polarization manipulation, which simultaneously alters the output polarization. This necessitates the use of linearly polarized input light aligned with the extraordinary axis of the liquid crystal layer, as any misalignment results in partial phase modulation and undesired zeroth-order diffraction. Moreover, SLMs require continuous electrical control and suffer from limited refresh rates, further restricting their dynamic performance. Other conventional methods, such as computer-generated holograms or fork gratings, usually produce fixed topological charges and do not allow dynamic tuning of beam properties. In contrast, the proposed moiré metasurface approach offers a compact, passive, and polarization-insensitive alternative with strong functional expandability. By rotating individual metasurface layers relative to each other, multiple beam parameters including beam direction, focal length, and topological charge can be continuously and jointly tuned. Notably, the proposed moiré metasurface approach is not limited to the control of vortex beams (OAM modes) alone. The underlying principle is equally applicable to other types of structured light, such as Bessel beams[69] or Airy beams.[47] Furthermore, the method is not restricted to continuous 3D spatial modulation; it can also be extended to dynamically control the beam order, diffraction length, and other characteristic parameters of structured light. Importantly, the proposed system operates in an electrode-free and mechanically static manner, offering high tunability in multiple degrees of freedom without relying on external electronics or moving parts. Its architecture is scalable and spectrally versatile, extending from the visible and near-infrared to the terahertz regime, and even to acoustic waves, making it well suited for compact and programmable optical and wave-based platforms. Nevertheless, the current implementation relies on mechanical tuning, and the modulation speed is inherently limited by the mechanical rotation system. In addition, the method requires simultaneous control over both rotation and alignment of multiple metasurface layers, placing high demands on the precision and stability of the adjustment mechanism. In future work, advanced imaging algorithms can be integrated into the system to enhance the quality of beam control, improve efficiency, and achieve dynamic adaptability, opening up new possibilities for complex scenarios such as 3D laser etching or 3D trajectory capture and manipulation of particles.

Acknowledgements

Project supported by the National Key Research and Development Program of China (Grant No. 2022YFF0706005), the National Natural Science Foundation of China (Grant Nos. 62275271, 62305387, 12272407, 62275269, and 62405037), the Natural Science Foundation of Hunan Province, China (Grant No. 2023JJ40683), the Foundation of NUDT (Grant No. ZK23-03), and Chongqing Natural Science Foundation (Grant Nos. CSTB2024NSCQ-MSX0581 and CSTB2024NSCQ-LZX0033).

References

[1] Rubinsztein-Dunlop H, Forbes A, Berry M V, Dennis M R, Andrews D L, Mansuripur M, Denz C, Alpmann C, Banzer P, Bauer T, Karimi E, Marrucci L, Padgett M, Ritsch-Marte M, Litchinitser N M, Bigelow N P, Rosales-Guzmán C, Belmonte A, Torres J P, Neely T W, Baker M, Gordon R, Stilgoe A B, Romero J, White A G, Fickler R, Willner A E, Xie G, McMorran B and Weiner A M 2017 *J. Opt.* **19** 013001
[2] Shen Y, Wang X, Xie Z, Min C, Fu X, Liu Q, Gong M and Yuan X 2019 *Light: Science & Applications* **8** 90
[3] Allen L, Beijersbergen M W, Spreeuw R J C and Woerdman J P 1992 *Phys. Rev. A* **45** 8185
[4] Molina-Terriza G, Torres J P and Torner L 2007 *Nat. Phys.* **3** 305
[5] Grier D G 2003 *Nature* **424** 810
[6] Barreiro J T, Wei T C and Kwiat P G 2008 *Nat. Phys.* **4** 282
[7] Xiao B, Zhao Y W, Cheng F J, Wang G W, Jiang W, Wang Y C, Hu J, Liang H J and Ma R 2024 *Chin. Phys. B* **33** 054209
[8] Yao J, Wu S M, Li X L, Liu J Q, Zhan Q W and Wang A T 2025 *Laser Photon. Rev.* **19** 2402290
[9] Lee W M, Yuan X C and Cheong W C 2004 *Opt. Lett.* **29** 1796
[10] Beijersbergen M W, Coerwinkel R P C, Kristensen M and Woerdman J P 1994 *Opt. Commun.* **112** 321
[11] Li R, Ren Y, Liu T, Wang C, Liu Z, Zhao J, Sun R and Wang Z 2022 *Chin. Opt. Lett.* **20** 120501
[12] Heckenberg N R, McDuff R, Smith C P and White A G 1992 *Opt. Lett.* **17** 221
[13] Zhang Z, Heng X, Wang J, Chen S, Wang X, Tong C, Li Z and Xuan H 2025 *Advanced Photonics Nexus* **4** 026011
[14] Forbes A, Dudley A and McLaren M 2016 *Adv. Opt. Photon.* **8** 200
[15] Liu Z, Liu Y, Ke Y, Liu Y, Shu W, Luo H and Wen S 2017 *Photon. Res.* **5** 15
[16] Shang Z, Fu S, Hai L, Zhang Z, Li L and Gao C 2022 *Opt. Express* **30** 34053
[17] Lyu Z, Wang P and Wang C 2023 *Chin. Phys. B* **32** 124209
[18] Wang A, Yu L, Li J and Liang X 2023 *Chin. Phys. B* **32** 044201
[19] Chen K, Ma Z Y and Hu Y Y 2023 *Chin. Phys. B* **32** 024208
[20] Yu N, Genevet P, Kats M A, Aieta F, Tetienne J P, Capasso F and Gaburro Z 2011 *Science* **334** 333
[21] Kim H, Yun H, Jeong S, Lee S, Cho E and Rho J 2025 *ACS Nano* **19** 3085
[22] Liu Z, Wang D, Gao H, Li M, Zhou H and Zhang C 2023 *Adv. Photon.* **5** 034001
[23] Wang H L, Zhang Y K, Cheng Y T, Zhang T Y, Zheng S, Cui T J and Ma H F 2025 *Laser & Photonics Reviews* **n/a** 2500057
[24] Chen Q, Huang X, Ju Z, Lin H, Tang H, Guo C, Fan F, Zhao X, Ma Y, Luo Y, Li W, Zhong W and Zhao D 2025 *Nano Lett.* **25** 4459
[25] Conrads L, Bontke F, Mathwieser A, Buske P, Wuttig M, Schmitt R, Holly C and Taubner T 2025 *Nat. Commun.* **16** 3698

[26] Gopakumar M, Lee G-Y, Choi S, Chao B, Peng Y, Kim J and Wetzstein G 2024 *Nature* **629** 791
[27] Lee J 2025 *Light: Science & Applications* **14** 150
[28] Liang H, Wong W C, An T and Li J 2025 *Adv. Photon.* **7** 026006
[29] Guo Y, Pu M, Zhao Z, Wang Y, Jin J, Gao P, Li X, Ma X and Luo X 2016 *ACS Photon.* **3** 2022
[30] Lin Z, Li X, Zhao R, Song X, Wang Y and Huang L 2019 *Nanophotonics* **8** 1079
[31] Kong L J, Zhang F, Cheng S and Zhang X 2025 *Laser & Photonics Reviews* **19** 2401608
[32] Wu H, Zeng Q, Wang X, Li C, Huang Z, Xie Z, He Y, Liu J, Ye H, Chen Y, Li Y, Fan D and Chen S 2023 *Nanophotonics* **12** 1129
[33] Dorrah A H and Capasso F 2022 *Science* **376** eabi6860
[34] He H, Yang H, Xie Z and Yuan X 2022 *Frontiers of Physics* **18** 12303
[35] Wang Z, Hu B, Li B, Liu W, Li X, Liu J and Wang Y 2016 *Materials Research Express* **3** 115011
[36] Bosch M, Shcherbakov M, Won K, Lee H S, Kim Y and Shvets G 2025 *ACS Photon.* **12** 728
[37] Sun S, Li J, Li X, Zhao X, Li K and Chen L 2024 *Microsystems & Nanoengineering* **10** 203
[38] Arbabi E, Arbabi A, Kamali S M, Horie Y, Faraji-Dana M and Faraon A 2018 *Nat. Commun.* **9** 812
[39] Bernet S and Ritsch-Marte M 2008 *Appl. Opt.* **47** 3722
[40] Bernet S, Harm W and Ritsch-Marte M 2013 *Opt. Express* **21** 6955
[41] Harm W, Bernet S, Ritsch-Marte M, Harder I, Lindlein N 2015 *Opt. Express* **23** 413
[42] Luo Y, Chu C H, Vyas S, Kuo H Y, Chia Y H, Chen M K, Shi X, Tanaka T, Misawa H, Huang Y Y and Tsai D P 2021 *Nano Lett.* **21** 5133
[43] Heide F, Fu Q, Peng Y and Heidrich W 2016 *Sci. Rep.* **6** 33543
[44] Song Y, Yuan J, Chen Q, Liu X, Zhou Y, Cheng J, Xiao S, Chen M K and Geng Z 2025 *PhotoniX* **6** 6
[45] Yin Y, Yang Y, Li T, Zhou Y, Wu Y, Huang S and Huang H 2021 *Opt. Lett.* **46** 2549
[46] Balli F, Sultan M A and Hastings J T 2020 *Proceedings of SPIE* (Bellingham: SPIE) 114602F
[47] Zhang J C, Wu G B, Chen M K, Liu X, Chan K F, Tsai D P and Chan C H 2023 *Sci. Adv.* **9** eadf8478
[48] Wang G, Zhou T, Huang J, Wang X, Hu B and Zhang Y 2022 *Photon. Res.* **11** 100
[49] Cui C, Liu Z, Hu B, Jiang Y and Liu J 2021 *J. Opt.* **24** 015004
[50] Shang S, Liu H, Meng H, Wang F, Yang X, Shou Q and Wei Z 2024 *Opt. Express* **32** 28370
[51] Ogawa C, Nakamura S, Aso T, Ikezawa S and Iwami K 2022 *Nanophotonics* **11** 1941
[52] Guo Y, Pu M, Ma X, Li X, Shi R and Luo X 2019 *Appl. Phys. Lett.* **115** 163103
[53] Li X, Cai X, Liu C, Kim Y, Badloe T, Liu H, Rho J and Xiao S 2024 *Opto-Electronic Advances* **7** 240085
[54] Yuan G Q, Li X R, Zhu X F, Yao J, Wei Q and Wu D J 2025 *Ultrasonics* **145** 107466
[55] Aieta F, Genevet P, Yu N, Kats M A, Gaburro Z and Capasso F 2012 *Nano Lett.* **12** 1702
[56] Zhang L, Zhang L, Xie R, Ni Y, Wu X, Yang Y, Xing F, Zhao X and You Z 2023 *Adv. Sci.* **10** 2300542
[57] Wei Y, Wang Y, Feng X, Xiao S, Wang Z, Hu T, Hu M, Song J, Wegener M, Zhao M, Xia J and Yang Z 2020 *Adv. Opt. Mater.* **8** 2000142
[58] Khorasaninejad M, Chen W T, Devlin R C, Oh J, Zhu A Y and Capasso F 2016 *Science* **352** 1190
[59] Khorasaninejad M, Zhu A Y, Roques-Carmes C, Chen W T, Oh J, Mishra I, Devlin R C and Capasso F J N l 2016 *Nano Lett.* **16** 7229
[60] Zhan A, Colburn S, Trivedi R, Fryett T K, Dodson C M and Majumdar A 2016 *ACS Photon.* **3** 209
[61] Wirth-Singh A, Fröch J E, Yang F, Martin L, Zheng H, Zhang H, Tanguy Q T, Zhou Z, Huang L, John D D, Stamenic B, Hu J, Gu T and Majumdar A 2025 *Light: Science & Applications* **14** 17
[62] Qian Y, Hu B, Du Z and Liu J 2021 *Opt. Express* **29** 26496
[63] Fan Z, Qian C, Jia Y, Feng Y, Qian H, Li E P, Fleury R, Chen H 2024 *Nat. Commun.* **15** 9416
[64] Ghahremani M, McClung A, Mirzapourbeinekalaye B and Arbabi A 2024 *Nat. Commun.* **15** 8864
[65] Matsushima K 2010 *Opt. Express* **18** 18453
[66] Byrnes S J, Lenef A, Aieta F and Capasso F 2016 *Opt. Express* **24** 5110
[67] Li X, Cai X, Liu C, Kim Y, Badloe T, Liu H, Rho J and Xiao S 2024 *Opto-Electronic Advances* **7** 240085
[68] Liang H, Martins A, Borges B H V, Zhou J, Martins E R, Li J and Krauss T F 2019 *Optica* **6** 1461
[69] Wang G, Zhou T, Huang J, Wang X, Hu B and Zhang Y J P R 2022 *Photon. Res.* **11** 100